Journal of Materials Science & Technology 31 (2015) 806–814

Contents lists available at ScienceDirect

Journal of Materials Science & Technology

journal homepage: www.jmst.org

Preparation and Microstructural Characterization of Activated Carbon-Metal Oxide Hybrid Catalysts: New Insights into Reaction Paths

A. Barroso-Bogeat*, M. Alexandre-Franco, C. Fernández-González, V. Gómez-Serrano

Department of Organic and Inorganic Chemistry, Faculty of Sciences, University of Extremadura, Avda. de Elvas s/n, E-06006 Badajoz, Spain

ARTICLE INFO

Article history:
Received 28 September 2014
Received in revised form
19 November 2014
Accepted 20 November 2014
Available online 12 June 2015

Key words:
Activated carbon
Metal oxides
Hybrid catalysts
Preparation
Microstructural characterization
X-ray diffraction

In catalysis processes, activated carbon (AC) and metal oxides (MOs) are widely used either as catalysts or as catalyst supports because of their unique properties. A combination of AC and MO nanoparticles in a single hybrid material usually entails both chemical and microstructural changes, which may largely influence the potential catalytic suitability and performance of the resulting product. Here, the preparation of a wide series of AC–MO hybrid catalysts is studied. Three series of such catalysts are prepared by support first of MO (Al_2O_3, Fe_2O_3, SnO_2, TiO_2, WO_3, and ZnO) precursors on a granular AC by wet impregnation and oven-drying at 120 °C, and by subsequent heat treatment at 200 or 850 °C in inert atmosphere. Both the chemical composition and microstructure are mainly investigated by powder X-ray diffraction. Yield and ash content are often strongly dependent on the MO precursor and heat treatment temperature, in particular for the Sn catalysts. With the temperature rise, trends are towards the transformation of metal hydroxides into metal oxides, crystallinity improvement, and occurrence of drastic composition changes, ultimately leading to the formation of metals in elemental state and even metal carbides. Reaction paths during the preparation are explored for various hybrid catalysts and new insights into them are provided.

1. Introduction

Nowadays, one of the most active research topics concerning carbon materials is their use in heterogeneous catalysis. In this field, the aforesaid materials can act either as catalysts in their own right or, more commonly, as a support of other catalytically active phases[1–5]. Among the great variety of carbon materials, activated carbon (AC, hereafter) is the most frequently selected one for the preparation of carbon-supported catalysts[2,6–9]. AC is an amorphous carbon material characterized by excellent textural properties (i.e., surface area, porosity, and pore size distribution) and surface chemistry. Some advantages of using AC are its chemical stability and thermal resistance. Another important factor is the possibility of preparing a catalyst with a tailored porous structure needed for a given reaction. Finally, the price of AC supports is usually lower than that of conventional supports, such as alumina or silica, and the catalytic phase can be easily recovered by burning the carbon support[1,10,11]. However, AC supports have some significant drawbacks, mainly associated with their use in hydrogenation reactions above 700 K and in reactions under oxygen atmosphere at temperatures above 500 K, as a consequence of the gasification of carbon atoms to yield methane and carbon dioxide, respectively[1,11].

Because of a number of properties, such as crystal and electronic structure, stoichiometry and composition, particle size, redox properties, acid-base character, and cation valence, metal oxides (MOs, henceforth) are also used either as catalysts or as catalyst supports for a great variety of applications, ranging from fuels and chemicals processing to environmental protection. Some catalytic applications of MOs include selective oxidation of hydrocarbons, methane oxidation, oxidative dehydrogenation of alkanes, metathesis of olefins, combustion of volatile organic compounds, CO_x hydrogenation, selective catalytic reduction, basic catalysis, and so on[12]. Among MO catalysts, those of transition metals occupy a predominant place due to their low-cost production, easy regeneration, and selective action[13].

Recently, there has been a growing interest and research activity in carbon-based materials as catalyst supports in reactions for the processing of biomass into chemicals and fuels[12]. More

* Corresponding author. Tel.: +34 924 289421; Fax: +34 924 271449.
E-mail address: adrianbogeat@unex.es (A. Barroso-Bogeat).

http://dx.doi.org/10.1016/j.jmst.2015.06.004

specifically, a wide range of hybrid materials based on MO nanoparticles supported on AC have been successfully tested as catalysts in fuels and chemicals processing. Some examples are Fe_2O_3, hydroxylation of benzene[14,15], dehydrogenation of propane[16], acylation of alcohols and amines[17], and so on; ZnO, desulphurization of bioethanol[18] and hot coal gas[19], biogas purification in hydrogen production systems[20]; WO_3, decomposition of isopropanol[21,22], isomerization of 1-butene[23], decomposition of methanol and ethanol[24], combustion of toluene[25], hydrogenation of ethylene[26]; SnO_2, low temperature oxidation of CO[27,28]; Al_2O_3, hydroprocessing and hydrodesulphurization processes[29,30].

Herein, using a commercial AC and a broadly varied series of MO (Al_2O_3, Fe_2O_3, SnO_2, TiO_2, WO_3, and ZnO) precursors, the preparation of AC–MO hybrid catalysts is studied. Since catalysis processes of industrial interest usually require heating at relatively high temperatures[11], at which physico-chemical properties of the catalyst may undergo modifications and thereby influence its catalytic behavior, three series of hybrid catalysts are prepared by heating under different conditions. Resulting catalysts are characterized in terms of their chemical composition and microstructure. Some respects of the performance of the MO precursors and the reaction paths during the preparation of the hybrid catalysts are also the object of a special attention. The textural characterization of these catalysts was previously reported elsewhere[13].

2. Experimental

2.1. Materials and reagents

A granular AC from Merck® (Darmstadt, Germany), 1.5 mm in average particle size (Cod. 1.02514.1000), as received without any further treatment, was used as support of Al_2O_3, Fe_2O_3, SnO_2, TiO_2, WO_3 and ZnO. Metal nitrates, which are readily soluble in water, as a rule were used as precursors of MOs. The employed precursors were $Al(NO_3)_3\cdot 9H_2O$, $Fe(NO_3)_3\cdot 9H_2O$, $SnCl_2\cdot 2H_2O$, $Na_2WO_4\cdot 2H_2O$ and $Zn(NO_3)_2\cdot 6H_2O$, all of them were purchased from Panreac® (Barcelona, Spain), being of reagent grade. As an exception to the rule, anatase powder (Aldrich®; Steinheim, Germany), less than 325 mesh average particle size, was used as TiO_2 precursor.

2.2. Preparation of AC–MO hybrid catalysts

The preparation of the AC–MO hybrid catalysts was carried out following the methods previously described in detail by Barroso-Bogeat et al.[13]. Accordingly, as a whole, three series of catalyst samples were prepared, i.e. three of these samples with each MO precursor, depending on heating conditions in the oven-drying and heat treatments. They were series 1: 120 °C, 24 h; series 2: 200 °C, 2 h; and series 3: 850 °C, 2 h. The codes assigned to the prepared catalysts are shown in Table 1. For comparison purposes, two samples were obtained by heating only AC, in the absence of any MO, under the same conditions as in the preparation of the AC–MO catalysts. Such samples are referred to in the text as AC200 and AC850. In order to prevent the adsorption of water, gases and vapors from the laboratory atmosphere, both the AC samples and the AC–MO hybrid catalysts after preparation were allowed to cool down to room temperature in inert atmosphere and kept in a desiccator prior to weighing and carrying out the powder XRD analyses.

Table 1
Preparation of the hybrid AC–MO catalysts

Precursor	Heat treatment temperature		
	120 °C	200 °C	850 °C
$Al(NO_3)_3\cdot 9H_2O$	A120	A200	A850
$Fe(NO_3)_3\cdot 9H_2O$	F120	F200	F850
$SnCl_2\cdot 2H_2O$	S120	S200	S850
TiO_2 (anatase)	T120	T200	T850
$Na_2WO_4\cdot 2H_2O$	W120	W200	W850
$Zn(NO_3)_2\cdot 6H_2O$	Z120	Z200	Z850

The yield of the preparation process of the AC samples and hybrid catalysts was estimated by the following expression:

$$\text{Yield}\ (\%) = \frac{M_f(g)}{M_i(g)}\cdot 100 \quad (1)$$

where M_i is the initial mass either of AC (i.e., 25 g) used in the impregnation treatment or of the samples of series 1 used in the subsequent heat treatment, whereas M_f is the mass of final product after oven-drying at 120 °C or heat-treating at 200 or 850 °C.

2.3. Characterization

2.3.1. Ash content

The ash content of AC, both AC heat-treated products, and hybrid catalyst samples was determined by incineration at 650 °C for about 12 h in air, using a muffle furnace (Selecta®). The soaking time at maximum heat treatment temperature was long enough to ensure that the material fraction contained in each sample was completely oxidized and transformed into gaseous products and residual ashes.

2.3.2. X-ray diffraction

The powder X-ray diffraction (XRD) patterns were recorded at room temperature in a D8 Bruker® Advance diffractometer with Cu $K\alpha$ radiation ($\lambda = 0.15406$ nm). Such patterns were obtained in the step scanning mode of 0.02° (2θ) and 0.5 s step^{-1} counting time, within the range of 10°–80°. Crystalline phases present in the samples were identified by comparing peak positions and intensities with JCPDS standard files and with data previously reported in literature.

The average crystallite size, D, was estimated for each of the main crystalline phases in the catalysts by applying the Scherrer equation[31] to their corresponding diffraction peaks:

$$D = \frac{K\lambda}{\beta\cos\theta} \quad (2)$$

where K is the so-called Scherrer constant ($K = 0.94$[31]), λ is the wavelength of the X-ray radiation, β denotes the full-width at half-maximum of the diffraction peak and θ is the characteristic Bragg angle of the crystalline phase.

3. Results and Discussion

3.1. Preparation of AC200 and AC850

The yield of the preparation process of AC200 and AC850 is around 97 and 95 wt.%, respectively. These high yield values show that AC had been previously heat-treated at high temperature during its manufacture and as a result the mass loss produced in its subsequent heat treatment is only of little significance.

3.2. Analysis of AC and AC samples

3.2.1. Ash content

In quality terms low ash content is usually recommended for activated carbons. Therefore, the ash content of 4.72 wt.% for AC (Table 2) is relatively high, which may be connected with the

Table 2
Yield and proximate analysis of AC, heat-treated AC samples and hybrid AC–MO catalysts

Sample	Yield / %	Ash / wt.%	Sample	Yield / %	Ash / wt.%	Sample	Yield / %	Ash / wt.%
AC	–	4.72	AC200	97	6.37	AC850	95	7.64
A120	102	7.11	A200	93	8.86	A850	90	5.68
F120	114	13.63	F200	94	13.55	F850	81	14.66
S120	149	27.31	S200	96	27.21	S850	68	2.34
T120	103	8.82	T200	96	8.05	T850	98	9.33
W120	106	9.46	W200	96	9.93	W850	95	11.54
Z120	103	9.73	Z200	91	9.45	Z850	84	6.18

feedstock and experimental method used in its preparation. On the other hand, the heat treatment of AC at 200 and 850 °C produces a significant increase in the ash content of the material, which is 6.37 wt.% for AC200 and 7.64 wt.% for AC850, because of the irreversible dehydration and partial devolatilization and thereby concentration of inorganic matter in AC200 and AC850.

3.2.2. Structural changes

To elucidate the extent to which the heat treatment of AC in inert atmosphere brings about changes in its crystalline structure, the powder XRD patterns were recorded for the raw AC and only AC850 (Fig. 1). The patterns show broad reflections of typically amorphous materials at $2\theta = 24°$ and $2\theta = 44°$[32,33]. The asymmetric diffraction band in the range of 2θ from 40 to 47° reveals the turbostratic structure resulted from a low crystallite ordering of both carbon samples[34]. The two peaks at the aforementioned 2θ values were assigned to the (002) and (100) crystallographic planes, respectively, of graphite. It was also reported that the (100) reflections arise from the honeycomb structure formed by sp^2 hybridized carbon atoms, while the broad (002) reflection is suggestive of small domains of coherent, parallel stacking of the graphene sheets[35]. Since a decrease in the interlayer spacing due to the increase in the height of crystallites for activated carbon was caused as a result of heat treatment at high temperatures and gave rise to a strong reflection at approx. 26°[34], the very sharp and intense reflection at $2\theta = 27°$ shown in the XRD patterns of AC and AC850 is ascribable to the microcrystalline structure of the samples. Fig. 1 also shows that the patterns recorded for AC and AC850 are similarly featured. Therefore, from these results it is evident that the heat treatment of AC at 850 °C does not appreciably modify its crystalline structure. It is well in agreement with previously reported results which showed that the influence of heat treatment temperature of a commercial activated carbon (Norit® R3-ex) on the interlayer spacing was small up to 1800 °C[34].

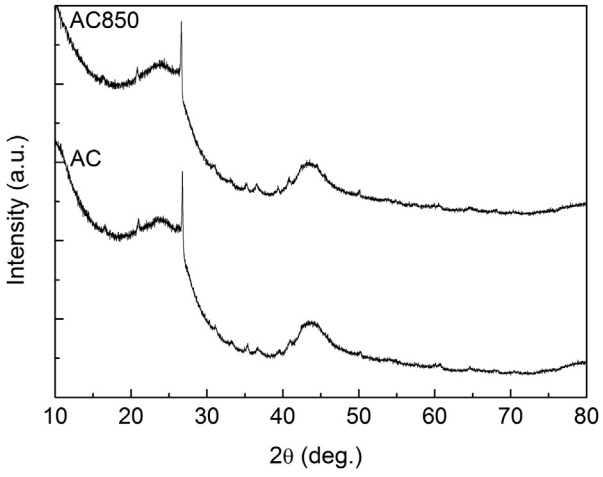

Fig. 1. Powder XRD patterns for AC and AC850.

3.3. Series 1

3.3.1. Yield

The yields obtained for the hybrid catalysts of series 1 (see data in Table 2) as a rule are significantly higher than 100%, as expected because the wet impregnation process entails the introduction of chemical species of the different precursors in the porous network of the carbon support by adsorption from the aqueous medium (i.e., solution or suspension), thus increasing the mass of the impregnated product as compared to the raw AC. Furthermore, yield is strongly dependent on the metal used in the preparation of the hybrid catalyst. It varies in the wide range from 102 % for A120 to 149 % for S120, and in the following order: S120 >> F120 > W120 > Z120 ≈ T120 > A120. The yield values demonstrate the effectiveness of the impregnation method. Impregnation of a porous solid such as AC depends on its adsorption capacity which, among other factors, is controlled by the diffusion of the adsorptive in pores of the adsorbent. This is particularly true for an adsorbent such as AC because typical activated carbons are essentially microporous solids and thereby diffusion in narrow pores must be more or less hindered and even prevented according to the size of the adsorptive ion or colloidal particle in the aqueous system. Of course, the size of the adsorptive depends not only on each metal but also on its speciation in the aqueous medium. Metal ions, especially those in a high oxidation state, in aqueous solution undergo hydrolysis by reaction (3):

$$M(H_2O)_n^{z+} + H_2O \leftrightarrow M(H_2O)_{(n-1)}OH^{(z-1)+} + H_3O^+ \quad (3)$$

For the sake of simplicity this reaction is often written as follows:

$$M^{z+} + H_2O \leftrightarrow M(OH)^{(z-1)+} + H_3O^+ \quad (4)$$

In this reaction, a proton from a water molecule in the coordination sphere of the metal ion is transferred to a water molecule in the solvent. Then, the hydrated cation behaves as a Brønsted acid and the water molecule as a Brønsted base. The hydrolysis of the Fe^{3+} ion begins at about pH 1 with formation of $Fe(OH)^{2+}$. Likewise, the species $Fe(OH)_2^+$, $Fe_2(OH)_2^{4+}$, and $Fe_3(OH)_4^{5+}$ were identified, usually at higher pH. The Al^{3+} ion can be hydrolyzed extensively to form solutions of polynuclear hydroxide complexes and very large polymeric or colloidal species. Mononuclear species $Al(OH)^{2+}$ and $Al(OH)_4^-$ are also formed, the former appearing above pH 3. Zn^{2+} hydrolyzes only sparingly in acid media to produce $Zn(OH)^+$ and $Zn_2(OH)_3^+$ before precipitation commences in the neutral region. In basic media, $Zn(OH)_4^{2-}$ and perhaps $Zn_2(OH)_6^{2-}$ are formed[36]. $SnCl_2$ is readily soluble in water (178 g $SnCl_2$/100 g H_2O at 25 °C[37]) and, depending on concentration, is prone to hydrolysis decomposing to the basic salt Sn(OH)Cl, which precipitates, plus HCl[38]. From the monotungstate ion (WO_4^{2-}), which is found in alkaline solutions down to a pH value of 8, formation of hexatungstate ($HW_6O_{21}^{5-}$) and other polynuclear species is possible with lowering pH. Finally, TiO_2

is found as colloidal particle (particle size lower than 44 μm) in the aqueous suspension.

From the above statements it follows that speciation as a rule is very different for the various metals. Even for the Fe^{3+} and Al^{3+} ions, which possess the same charge and a rather similar radius, hydrolytic products may differ greatly in their size. Furthermore, hydrolysis is also a function of solution concentration, pH, and so on. Moreover, it is probable that various chemical species of the same metal take part simultaneously in the adsorption process, thus contributing to the mass increase in the preparation of the hybrid catalysts. In any event it is worth mentioning that a correlation of yield with the ionic radius is not observed. Such a radius (in Å) varies by Sn^{2+} (0.93) > Zn^{2+} (0.83) > Fe^{3+} (0.67) > Al^{3+} (0.57)[39] (i.e., the radius values are omitted for the metals which were not found as cations in the impregnation solution) and therefore diffusion should be more and less hindered for Sn^{2+} and Al^{3+}, respectively, which is the opposite behavior to the expected one according to the yield values obtained for S120 and A120 (Table 2). However, yield is lower for A120, T120, and W120, which were prepared by impregnation with adsorptive solutions that might contain larger size species than for the rest of samples.

Another likely factor with influence on the mass of sample is the metal density. This factor is very important as metals range widely between heavy and light metals. For the here used metals the density (g cm^{-3}) varies by the sequence W (19.3) > Fe (7.87) > Zn (7.14) > Sn (6.52; white and grey Sn average value) > Ti (4.51) > Al (2.70)[37], which is in line with the yield values obtained for T120 and A120. For F120 and Z120 the correlation is also good. Because of its much greater density, the presence of W in W120 should be smaller than that expected from the relatively high value of yield for this sample (i.e., 106 %). By contrast, the opposite applies to the presence of Sn in S120, which should be higher than that reflected by the yield value. Moreover, another factor contributing to the smaller presence of W in W120 could be the fact that the MO precursor (i.e., WO_4^{2-} ion) has a lower metal to oxygen atomic ratio as compared to the other precursors.

3.3.2. Ash content

Data of the ash content in Table 2 also show a marked influence of the metal, varying by the sequence S120 >> F120 > Z120 > W120 > T120 > A120 > AC, and in the wide range of 7.11 wt.% for A120 to 27.31 wt.% for S120. As expected, the ash content is particularly high for S120. Since it is 4.72 wt.% for AC, it can be easily estimated that the increase produced in the ash content is at least ≈51 % for A120. The variation sequence for the ash content is similar to that of yield, except for W120, Z120 and T120 as the ash content is higher for Z120 whereas the yield is for W120. Both yield and ash content are higher for S120 than for F120 and lower for A120. Also, it should be taken into account that as a result of the incineration of the hybrid catalysts to become ashes, MOs of different stoichiometry may be formed and that this should affect the mass balance. Nevertheless, the influence of the MO stoichiometry on the mass of product should be less marked than that of the metal density as the atomic mass of oxygen is smaller than for the metals.

3.3.3. Structural changes

The powder XRD patterns registered for the hybrid catalysts of series 1 have been omitted for the sake of brevity as they are very similarly shaped to the pattern recorded for the pristine AC. The analysis of such diffractograms by suitable software reveals the presence of the crystalline phases compiled in Table 3, together with their corresponding average crystallite size estimated by applying the Scherrer formula (Eq. (2)). The supported phases are essentially metal hydroxides and oxides grown in crystallites, with a mean size ranging from 1.06 to 60.02 nm. The metal phases exhibit a highly amorphous structure as broad and very low intensity reflection peaks are generally observed in the diffractograms. As the only exception to the rule, the pattern for T120 features several sharp and intense peaks, which prove the presence of some crystalline phase in this catalyst sample. It must be TiO_2-anatase, which is used directly in the preparation of T120 and has a relatively crystalline structure. The patterns of A120, F120 and Z120 exhibit broad reflections ascribable to hydroxides such as bayerite (α-$Al(OH)_3$), goethite (α-FeO(OH)), and wülfingite (ε-$Zn(OH)_2$), whereas the metal phases detected in S120, T120 and W120 include oxides such as cassiterite (SnO_2), anatase (TiO_2), and tungstite ($WO_3 \cdot H_2O$). These reflection assignments are in accord with the metal phases reported in several previous works concerning the preparation of AC–MO hybrid materials also by wet impregnation of activated carbons for their use in photocatalysis and industrial catalysis. Thus, the preparation of such materials was undertaken by using aqueous solutions of $Fe(NO_3)_3$[40–42], $SnCl_2$[43] and $(NH_4)_2W_2O_4$ or Na_2WO_4[21,22].

The powder XRD pattern for Z120 also shows reflection peaks attributable to ZnO of 60.02 nm average crystallite size. Such a zinc phase is likely formed by partial dehydration of $Zn(OH)_2$, which is the predominant phase in Z120. In fact, experimental data have confirmed that the six $Zn(OH)_2$ polymorphs undergo the following dehydration reaction in the range from 70 to 140 °C[44], leading to ZnO:

$$Zn(OH)_2 + \Delta \leftrightarrow ZnO + H_2O \quad (5)$$

The larger crystallite size of ZnO may be related to the formation of coarse Zn-based crystals[45] as a result of the successive wet impregnation and oven-drying stages.

As a summary, wet impregnation followed by oven-drying at 120 °C results in the support on AC of metal hydroxides and oxyhydroxides or metal oxides depending on whether metal nitrates or other precursors are used as the impregnation agent. Therefore, in accord with the objectives of the present work, it was necessary to carry out a subsequent heat treatment at higher temperature (i.e., 200 or 850 °C) for the feasible transformation of the metal hydroxides and oxyhydroxides into MOs.

3.4. Series 2

3.4.1. Yield

For the hybrid catalysts of series 2 (data in Table 2), yield varies by AC200 > T200 ≈ S200 ≈ W200 > F200 > A200 > Z200, and in the narrow range from 91% for Z200 to 97% for AC200. Therefore, the subsequent heat treatment of the 120 °C hybrid catalysts at 200 °C does not produce significant mass decreases. The mass loss is higher for F200, A200, and particularly for Z200, which is attributable to an additional water removal by dehydration of the corresponding metal hydroxides. Furthermore, as expected, the mass loss is almost negligible for S120, T120 and W120, as the yield values are 96% for this series of catalysts.

3.4.2. Ash content

Comparison of the ash contents obtained for the hybrid catalysts of series 1 and 2 (data in Table 2) reveals that the ash contents as a rule are quite similar. For example, the ash content is 13.63 wt.% for F120 and 13.55 wt.% for F200. Therefore, from these results it becomes also apparent the small effect of the heat treatment of the 120 °C catalysts at 200 °C on the mass of sample.

3.4.3. Structural changes

The powder XRD patterns recorded for the hybrid catalysts of series 2 in Fig. 2, as for most catalysts of series 1, do not display

Table 3
Crystalline phases, and average crystallite sizes, for each of the prepared AC–MO catalysts

Catalyst	Crystalline phase	Crystal size / nm	Catalyst	Crystalline phase	Crystal size / nm	Catalyst	Crystalline phase	Crystal size / nm
A120	Bayerite ($Al(OH)_3$)	1.06	A200	Alumina (Al_2O_3)	1.88	A850	Corundum (α-Al_2O_3)	2.06
F120	Goethite (α-FeO(OH))	2.32	F200	Hematite (α-Fe_2O_3)	3.22	F850	Hematite (α-Fe_2O_3)	36.60
				Goethite (α-FeO(OH))	3.17			
				Magnetite (Fe_3O_4)	6.19		Maghemite (γ-Fe_2O_3)	15.11
				Feroxyhyte (δ-FeO(OH))	6.85			
S120	Cassiterite (SnO_2)	3.95	S200	Cassiterite (SnO_2)	4.05	S850	Cassiterite (SnO_2)	36.16
				Romarchite (SnO)	5.07		Tin (β-Sn)	89.62
T120	Anatase (TiO_2)	3.49	T200	Anatase (TiO_2)	3.53	T850	Anatase (TiO_2)	2.31
							Rutile (TiO_2)	1.86
W120	Tungstite ($WO_3 \cdot H_2O$)	3.64	W200	Tungsten oxide (WO_3)	2.37	W850	Tungsten (α-W)	48.36
				Tungstite ($WO_3 \cdot H_2O$)	3.05		Tungsten Carbide ($W_6C_{2.54}$)	3.67
							Iron tungsten carbide (Fe_6W_6C)	29.53
Z120	Zinc oxide (ZnO)	60.02	Z200	Zinc oxide (ZnO)	20.80	Z850	Zinc oxide (ZnO)	69.38
	Wülfingite (ε-$Zn(OH)_2$)	29.9		Wülfingite (ε-$Zn(OH)_2$)	1.89			

sharp and intense reflection peaks. Therefore, the different metal phases supported on AC after heat-treating at 200 °C are still essentially amorphous structures. Again, only the diffractogram for T200 in Fig. 2(d) shows well-defined peaks, which are attributable to the crystalline structure of the starting TiO_2-anatase powder employed in its preparation.

Comparison of peak positions and intensities in the aforesaid powder XRD patterns with standard files and data previously reported in literature indicates that the metal phases present in the hybrid catalysts of series 2 are predominantly oxides. Such phases and their average crystallite size, as calculated by the Scherrer equation, are collected in Table 3. The diffractogram for A200 in Fig. 2(a) displays a set of weak and broad reflections ascribable to amorphous Al_2O_3 of a very small crystallite size (i.e., ~1.88 nm), which is well in agreement with previous results[46]. This amorphous Al_2O_3 phase may be formed by dehydration of bayerite, α-$Al(OH)_3$, which is the predominant phase in A120. In fact, the heat treatment of the various $Al(OH)_3$ polymorphs, including bayerite, at different temperatures has been long applied to prepare aluminas, some of them metastable, with suitable physico-chemical and textural properties for their application as catalysts or catalyst supports[47]. A full scheme of the possible dehydration paths of aluminum hydroxides, including the resulting transition aluminas and starting temperatures of each conversion, has been reported by Digne et al.[48]. The conversion of bayerite into η-Al_2O_3 occurs at around 230 °C, which is a somewhat higher temperature than 200 °C. The lower transition temperature for bayerite in A120 may be connected with its small particle size (i.e., ~1.06 nm) as Du et al.[49] have recently pointed out that the size-reducing of bayerite by grinding leads to a decrease in the onset temperature of its transformation into Al_2O_3.

Reflection peaks attributable to several iron-containing phases, including hematite (α-Fe_2O_3), goethite (α-FeO(OH)), magnetite (Fe_3O_4) and feroxyhyte (δ-FeO(OH)), are detected in the powder XRD pattern registered for F200 (Fig. 2(b)). The estimated average crystallite sizes for both hematite and goethite phases are small, i.e. ~3.2 nm, and very similar, thus indicating that α-FeO(OH) directly transforms into α-Fe_2O_3 by the following dehydration reaction:

$$2\ \alpha\text{-FeO(OH)} + \Delta \rightarrow \alpha\text{-}Fe_2O_3 + H_2O \quad (6)$$

which is promoted by the heat treatment of F120 at 200 °C. This transformation has been reported to occur through a mechanism involving removal of water molecules and rearrangement of iron ions and protons by a cation transfer process across the interface into the developing oxide layer, without the formation of any intermediate phase[50–52]. However, Lima-de-Faria[53] noticed the formation of magnetite as intermediate product during the goethite to hematite transformation performed under vacuum or inert atmosphere. In fact, small amounts of magnetite grown in crystallites with an average size of ~6.2 nm are also detected in the case of F200. A comprehensive review on the possible interconversions among the various iron oxides under different conditions was reported by Cornell and Schwertmann[54].

The powder XRD pattern for S200 in Fig. 2(c) shows reflection peaks ascribable to romarchite (SnO) and cassiterite (SnO_2) with average crystallite sizes ranging from 4 to 5 nm. Since SnO_2 is the only tin phase detected in S120, it becomes clear that SnO_2 is partially reduced during the heat treatment of S120 at 200 °C in inert atmosphere, giving metastable SnO as the main product. The lower tin oxide is a graphite-like black powder which is very unstable; in the absence of air it dissociates into SnO_2 and Sn[55]. Platteeuw and Meyer[56] showed experimentally that solid SnO is unstable and decomposes into Sn and SnO_2 at temperatures above 300 °C. SnO disproportion occurs in two successive steps with formation of the intermediate mixed oxide Sn_3O_4[57]:

$$4\ SnO \rightarrow Sn_3O_4 + Sn \quad (7)$$

$$Sn_3O_4 \rightarrow 2\ SnO_2 + Sn \quad (8)$$

The pattern for W200 in Fig. 2(e) reveals the presence of tungstite ($WO_3 \cdot H_2O$) and tungsten trioxide (WO_3) phases in this catalyst. WO_3 appears as a dehydration product of tungstite that is the predominant phase in W120, according to literature[58,59]. A complete dehydration of $WO_3 \cdot H_2O$ is not reached, as evidenced by the residual tungstite remaining in W200. Surprisingly, this dehydration leads to the formation of metastable hexagonal WO_3 (h-WO_3, hereafter), first reported by Gerand et al.[60], instead of to the typical monoclinic structure which is stable at temperatures between 17 and 320 °C[61]. This finding might be of major relevance, in view of the potential applications of h-WO_3 in catalysis, hydrogen intercalation, electrochromic devices, humidity and gas sensors, and so on[58,59]. Several of these applications are related to the open structure of this WO_3 polymorph, consisting of large channels along the hexagonal axis[62]. Moreover, the tiny crystallite size estimated for $WO_3 \cdot H_2O$ and WO_3 phases (3.05 and 2.37 nm, respectively) are consistent with those

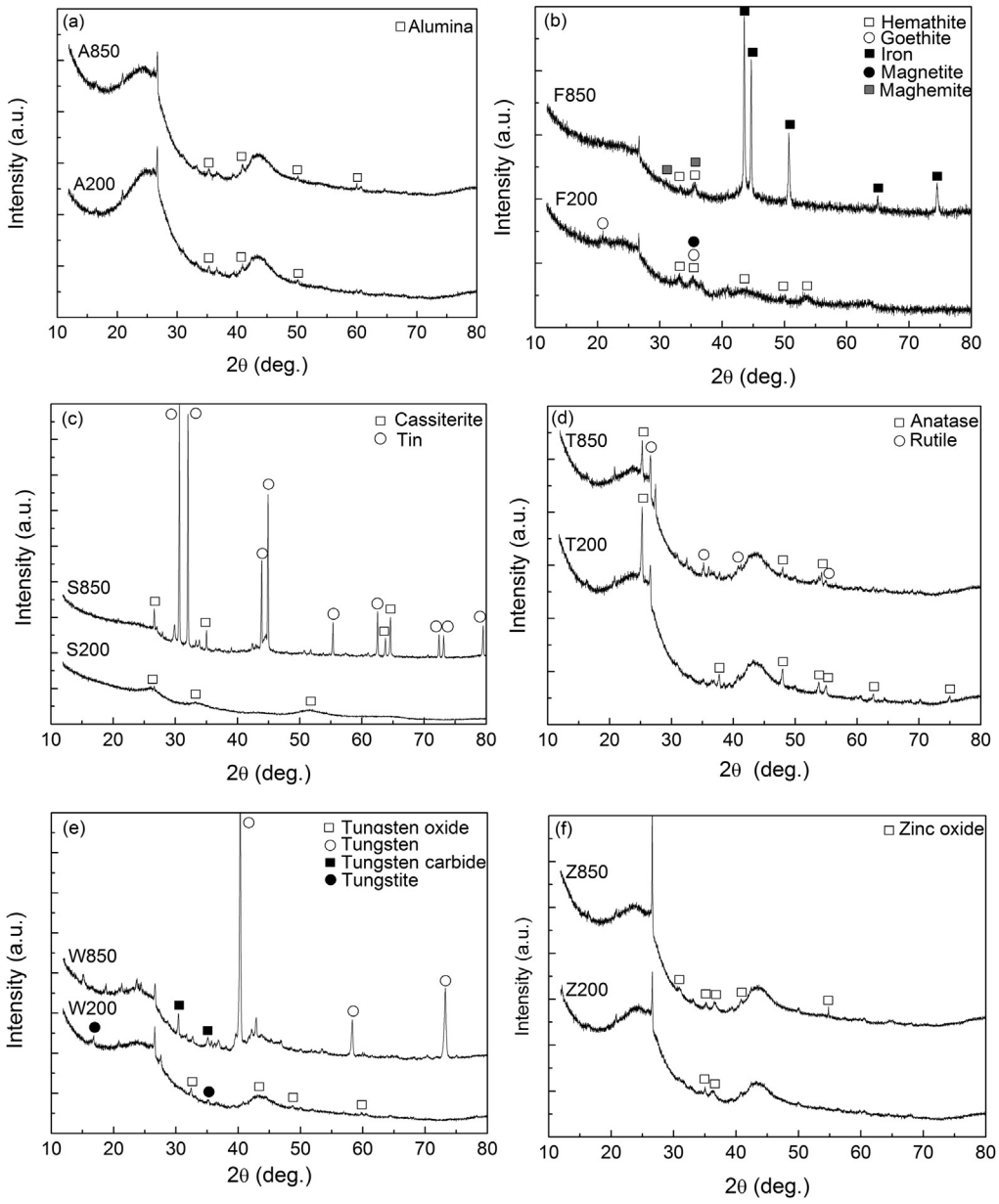

Fig. 2. Powder XRD patterns for AC–MO catalysts prepared by heat treatment at 200 and 850 °C.

previously obtained by Pérez-Cadenas et al.[21] for AC-tungsten oxide catalysts prepared by impregnation with $(NH_4)_2WO_4$, which were smaller than 4 nm.

The diffractogram for Z200 in Fig. 2(e) shows that the metal phases present in this hybrid catalyst are mainly ZnO, grown in the form of zincite, and also residual amounts of wülfingite (ε-$Zn(OH)_2$). As for A200 and F200, ZnO is surely formed by dehydration of $Zn(OH)_2$ present in Z120. Nevertheless, an important difference in the thermal behavior of Z120 as compared to A120 and F120 is that in the case of Z120 the dehydration process starts at a temperature as low as 120 °C, whereas for A120 and F120 it is only significant when heating at 200 °C. Moreover, the larger crystallite size of ZnO in Z200 (~20.80 nm) than of Al_2O_3 and α-Fe_2O_3 in A200 and F200 (1.88 and 3.22 nm, respectively) suggests that sintering of ZnO crystallites occurs when this metal oxide is heat-treated at 200 °C under inert atmosphere.

3.5. Series 3

3.5.1. Yield

For the hybrid catalysts of series 3 the yield (see Table 2) varies in the wide range from 68% for S850 to 98% for T850, and in the following order: T850 > W850 ≈ AC850 > A850 > Z850 > F850 > S850. Since yield is 95% for AC850 (Table 2), mass losses greater than 5% may be considered mainly due to transformations and chemical reactions undergone by the metal phases present in the 120 °C hybrid catalysts as a result of calcination at 850 °C. In fact, the lower yields for F850 and S850 have been ascribed to the reduction of the metal oxides by the carbon support to give the metals in elemental state. Thus, a significant mass of the AC support is consumed in the process with release of carbon oxides. Such reduction processes will be extensively discussed below. On the other hand, the highest yield value for T850 is not surprising, because T120 is directly prepared from TiO_2-anatase and

thus the changes produced by the heat treatment at 850 °C are of little significance.

3.5.2. Ash content

Comparison of the ash contents obtained for the hybrid catalysts of series 3 (Table 2) with those for the respective catalyst samples of series 1 and 2 clearly shows that the heat treatment of the 120 °C hybrid catalysts at 850 °C causes more or less noticeable changes in the inorganic matter content depending on the catalyst sample. For the catalysts containing Al, Sn and Zn oxides, an important reduction in the ash content occurs as a result of increasing the heat treatment temperature from 200 to 850 °C. The effect on the content of inorganic matter is much stronger for S850 than that for A850 and Z850. As seen below, carbothermic reduction of some MOs occurs during the heat treatment at 850 °C. The latter reaction gives rise to the formation of gaseous products and elemental metals, which undergo vaporization provided that melting point is below 850 °C[13]. The melting point of Zn is 419.7 °C and that of Sn (white) is 231.9 °C. Also, Al melts at 660.5 °C[37]. By contrast, inorganic content becomes slightly higher with increasing heat treatment temperature for the catalysts containing Fe, Ti and W oxides. Fe and W oxides also transform to elemental Fe and W, giving off CO[13]; however, the melting points of Fe and W are as high as 1535 and 3407 °C, respectively[37].

3.5.3. Structural changes

Powder XRD patterns registered for the AC–MO hybrid catalysts prepared by heat treatment at 850 °C are also shown in Fig. 2, together with those obtained for their counterparts of series 2 for comparison. The metal phases detected from each of these diffractograms and the average crystallite sizes are gathered in Table 3. As a rule sharper and more intense reflection peaks are registered in most of the patterns obtained for the catalysts of series 3, which are ascribable to a variety of MO phases exhibiting a high crystallinity. Therefore, the temperature rise from 200 to 850 °C in the preparation of the hybrid catalysts leads to a development of crystallinity and an increase of size for the MO crystallites supported on AC[46]. Such behavior is clearly illustrated by the diffractograms registered for F200 and F850 in Fig. 2(b). In addition, XRD results also suggest that the carbon support is able to reduce some of the supported MOs to the corresponding metals and even carbides, as a consequence of the heat treatment at 850 °C. These chemical transformations probably occur in the preparation of F850, S850 and in special W850[21,44], as revealed by the presence in the patterns of reflection peaks attributable to elemental Fe, Sn, and W. Reduction reactions involved in these processes are thermodynamically favorable at temperatures as high as 850 °C in inert atmosphere, according to the corresponding Ellingham diagrams[63,64]. Thus, the reduction of Fe_2O_3, SnO_2 and WO_3 begins at temperatures of about 680, 620 and 720 °C, respectively, which are far below 850 °C. By contrast, the reduction of Al_2O_3, TiO_2 and ZnO by carbon occurs only when heating temperatures are far above 850 °C, i.e. 2050, 1780 and 1180 °C, and consequently Al, Ti and Zn are not detected in the diffractograms obtained for A850, T850 and Z850.

Strikingly, the XRD pattern for A850 reveals the presence of α-Al_2O_3 (corundum) in this hybrid catalyst, in spite that this alumina polymorph is only formed at temperatures above 1200 °C. Similarly to A200, such an alumina phase is assumed to be formed by dehydration of bayerite when A120 is heated in the preparation of A850. However, it is worth mentioning that while only an amorphous Al_2O_3 phase is obtained by heating at 200 °C, the heat treatment at 850 °C results in crystalline α-Al_2O_3, which is the most stable alumina polymorph. According to Digne et al.[48], this conversion route involves the formation of at least two other metastable transition aluminas, named as η-Al_2O_3 and θ-Al_2O_3. The sequence followed in the transformation of bayerite with the temperature increase can be schemed as follows:

$$\alpha - Al(OH)_3 \xrightarrow{230\ ^\circ C} \eta - Al_2O_3 \xrightarrow{850\ ^\circ C} \theta - Al_2O_3 \xrightarrow{1200\ ^\circ C} \alpha - Al_2O_3 \quad (9)$$

Perhaps, the formation of α-Al_2O_3 during the preparation of A850 is likely connected with the small crystallite size of the bayerite present in A120. Thus, as previously stated, recent studies conducted by Du et al.[49] have indicated that the size-reducing of bayerite by mechanical grinding accelerates its phase transition to stable α-Al_2O_3. The onset of phase transition occurs already at 300 °C, around 900 °C lower than in the unground state. In this case the transition sequence is:

$$\alpha\text{-}Al(OH)_3 \rightarrow \gamma\text{-}AlO(OH) \rightarrow \gamma\text{-}Al_2O_3 \rightarrow \alpha\text{-}Al_2O_3 \quad (10)$$

which suggests that the formation of the aforesaid η-Al_2O_3 and θ-Al_2O_3 transitional phases is suppressed under these conditions. The final thermal decomposition product is uniform and disperse α-Al_2O_3 nanoparticles with a narrow size distribution. Furthermore, the rise of heat treatment temperature from 200 to 850 °C also produces a slight increase in the average crystallite size of Al_2O_3, i.e. from 1.88 to 2.06 nm.

Three iron phases are identified in F850 (Fig. 2(b)). They are two stable Fe_2O_3 polymorphs (i.e., hematite, α-Fe_2O_3 and maghemite, γ-Fe_2O_3) with rhombohedral and cubic structures, respectively, and α-Fe (body-centred cubic structure). The reflection assignments to such iron-containing phases are in good agreement with the results obtained in previous studies of preparation of AC-iron oxide hybrid catalysts[65–68]. Concerning F120, hematite must be formed by direct dehydration of goethite. The formation of maghemite may be striking since goethite only transforms directly into maghemite when heating in air atmosphere and in the presence of organic matter[54]. On the other hand, elemental Fe is likely formed through the reduction of hematite by the carbon support, usually referred to as carbothermic reduction, whose mechanism has been investigated in detail by Yang et al.[69] in carbon-hematite composites. The reduction proceeds through a complex mechanism involving various stages associated with the following reactions and temperatures[64]:

$$3\ Fe_2O_3 + C \leftrightarrow 2\ Fe_3O_4 + CO\ (T > 250\ ^\circ C) \quad (11)$$

$$Fe_3O_4 + C \leftrightarrow 3\ FeO + CO\ (T > 710\ ^\circ C) \quad (12)$$

$$FeO + C \leftrightarrow Fe + CO\ (T > 810\ ^\circ C) \quad (13)$$

Although gases such as CO are reducing agents at lower temperatures than C does, such gases should be continuously carried by the N_2 stream (flow rate = 100 mL min^{-1}) during the preparation of F850, and therefore the reduction of iron oxides by CO to a significant extent seems to be littler probable under the heating conditions of preparation of F850.

The diffractogram for S850 displays several reflection peaks ascribable to Sn and SnO_2 (Fig. 2(c)). Therefore, the presence of these phases in S850 and also the absence of SnO from it are consistent with the thermal decomposition of SnO, as seen above. According to Eqs. (7) and (8), the thermal decomposition of SnO should give rise to equimolar quantities of Sn and SnO_2. However, the S850 pattern shows a greater presence of Sn than of SnO_2. A Sn increase at the same time as SnO_2 decreases is provided by the direct carbothermic reduction of solid SnO_2 by solid C, which takes place at temperatures above 630 °C[55]:

$$SnO_2 + C \leftrightarrow Sn + CO_2\ (T > 630\ ^\circ C) \quad (14)$$

and that is important only in the absence of gaseous reaction products[70]. However, it should be also pointed out that the melting point of Sn (white) is 231.9 °C and the boiling point is 2602 °C[37]. Therefore, not only because of reaction (14) but also of Sn vaporization the mass of S120 decreases in the preparation of S850, as reflected by the low yield and ash content obtained for S850 (Table 2). Moreover, the small width and high intensity of the diffraction peaks reveal that the metal phases supported on AC possess a large crystallite size and a high crystallinity. The crystallite size is 89.62 nm for Sn and 36.16 nm for SnO_2.

As far as T850 is concerned, the presence of rutile is detected in the powder XRD pattern (Fig. 2(d)). Probably, rutile originates from anatase by a phase transition between both TiO_2 phases, which has been reported to occur in the temperature range 600–700 °C for TiO_2-carbon hybrid catalysts[71,72]. Such a transition seems to be very slow and hence incomplete after 2 h of heat treatment at 850 °C, as evidenced by the presence of reflection peaks attributable to anatase in the T850 diffractogram. Thus, the composition of the TiO_2 in T850 renders this hybrid material very suitable to be tested in photocatalysis, since it has been demonstrated that TiO_2-containing photocatalysts exhibit better performances when the TiO_2 comprises a mixture of anatase and rutile-type structures, in a similar way to the commercial and worldwide used photocatalyst Degussa® P25 (25% rutile-75% anatase)[73]. The average crystallite size is small for the anatase and rutile phases, i.e. ~2.31 nm for anatase versus ~1.86 nm for rutile. This reduction of crystallite size may be considered as a direct consequence of the aforesaid phase transition, which entails a rearrangement of ions in anatase lattice to yield the more compact structure of rutile, thus resulting in a higher density and lower volume. The density is 3.9 g cm^{-3} for the anatase phase[74] and 4.25 g cm^{-3} for the rutile phase[75].

Reflection peaks ascribable to either WO_3 or other tungsten oxides are not detected in the XRD pattern obtained for W850 (Fig. 2(e)). Conversely, metallic W and also several tungsten carbides of variable stoichiometry, such as WC and $W_6C_{2.54}$, are identified in this catalyst. These results, together with those obtained for W200, suggest that during the heat treatment of W120 in the preparation of W850 the total amount of tungstite in a series of successive stages is dehydrated to WO_3, reduced by the carbon support to metallic W, and reacted with the carbon support yielding different tungsten carbides. Moreover, the phases detected in W850 are in line with those previously found by Álvarez-Merino et al.[22] for AC-tungsten hybrid catalysts prepared by wet impregnation with $(NH_4)_2WO_4$ and subsequent heat treatment at 950 °C under inert atmosphere. The absence of tungsten oxides in W850 reveals that the reduction of WO_3 is complete when heating at 850 °C. Likely, it proceeds in a single step to metallic W, and not in various stages with formation as intermediates of WO_2 and other tungsten oxides exhibiting O to W atomic ratios between 2 and 3, in contrast to the findings of Venables and Brown[76,77]. Such a direct carbothermic reduction may be schematized by the following overall reaction[78]:

$$WO_3 + 3C \leftrightarrow W + 3\ CO\ (T > 700\ ^\circ C) \quad (15)$$

and has been explained on the basis of a high dispersion of WO_3 on the AC surface[22]. Probably, the reduction of WO_3 is followed by sintering of W, in view of its large crystallite size (~48.36 nm). The resulting metallic W, which is the predominant phase supported on AC in W850, should further react with the carbon support to give the aforementioned tungsten carbides:

$$WO_3 + 4C \leftrightarrow WC + 3\ CO \quad (16)$$

This reaction, so-called carburization, may also be a simple method to obtain tungsten carbides dispersed on a large surface carbon support, with many applications in catalysis and other fields.

Finally, by comparing the XRD patterns for samples Z200 and Z850 in Fig. 2(f), it follows that the increase in the heat treatment temperature of Z120 from 200 to 850 °C does not lead to the formation of crystalline zinc phases other than zincite, which had been detected in Z200. Nevertheless, it is worth mentioning that, as the only remarkable effect, the heat treatment of Z120 at the highest temperature results in the formation of zincite nanoparticles with a large size and higher crystallinity. The mean crystallite size increases from 20.80 to 69.38 nm.

4. Conclusions

Using a typical amorphous AC with 4.72 wt.% ash content as the catalyst support for several MOs, the effectiveness of the wet impregnation method is often strongly dependent on both the MO precursor and heat treatment temperature. For the 120 °C catalysts, the yield ranges between 102 and 149%, and varies by Sn >> Fe > W > Ti ≈ Zn > Al. The ash content varies similarly to the yield of the impregnation process. For the 200 °C catalysts, the yield ranges between 91% and 96% and the ash content undergoes only slight changes, as compared to the 120 °C catalysts. In the case of the 850 °C catalysts, the yield varies between 81% and 98%. The ash content decreases for the Al_2O_3, SnO_2 and ZnO catalysts and, in contrast, increases for the Fe_2O_3, TiO_2 and WO_3 catalysts. For the SnO_2 catalyst the ash content is as low as 2.34 wt.%. In the 120 °C catalysts, highly amorphous metal hydroxides such as bayerite (α-$Al(OH)_3$), goethite (α-FeO(OH)), and wülfingite (ε-$Zn(OH)_2$), and metal oxides like cassiterite (SnO_2) and tungstite ($WO_3 \cdot H_2O$) have been identified. They grow in crystallites of size ranging between 1.06 and 60.02 nm. Crystallinity is only observed in the case of the TiO_2 catalyst because of the TiO_2-anatase powder directly used in its preparation. Further dehydration by heating at 200 °C results in more crystalline phases with predominance of metal oxides such as Al_2O_3, α-Fe_2O_3, F_3O_4, SnO, SnO_2, WO_3, and ZnO. A variety of high crystallinity metal oxide phases is formed at 850 °C. At this heat treatment temperature, some metal oxides are reduced by the carbon support to metals in elemental state and even to metal carbides.

Acknowledgements

Financial support by Gobierno de Extremadura and European FEDER Funds is gratefully acknowledged. A. Barroso-Bogeat thanks Spanish Ministerio de Educación, Cultura y Deporte for the concession of a FPU grant (AP2010-2574).

References

[1] A. Barroso-Bogeat, C. Fernández-González, M. Alexandre-Franco, V. Gómez-Serrano, in: J.F. Kwiatkowski (Ed.), Activated Carbon: Classifications, Properties and Applications, Nova Science Publishers, New York, 2011, pp. 297–318.
[2] L.R. Radovic, F. Rodríguez-Reinoso, in: P.A. Thrower (Ed.), Chemistry and Physics of Carbon, Marcel Dekker, New York, 1997, pp. 243–358.
[3] J.L. Figueiredo, J. Mater. Chem. A 1 (2013) 9351–9364.
[4] J.L. Figueiredo, M.F.R. Pereira, Catal. Today 150 (2010) 2–7.
[5] J.L. Figueiredo, M.F.R. Pereira, in: P. Serp, J.L. Figueiredo (Eds.), Carbon Materials for Catalysis, John Wiley & Sons Inc., Hoboken, New Jersey, 2009, pp. 177–217.
[6] V. Calvino-Casilda, A.J. López-Peinado, C.J. Durán-Valle, R.M. Martín-Aranda, Catal. Rev. Sci. Eng. 52 (2010) 325–380.
[7] H. Jüntgen, Fuel 65 (1986) 1436–1446.
[8] E. Auer, A. Freund, J. Pietsch, T. Tacke, Appl. Catal. A 173 (1998) 259–271.

[9] Y. Yang, K. Chiang, N. Burke, Catal. Today 178 (2011) 197–205.
[10] H. Marsh, F. Rodríguez-Reinoso, Activated Carbon, Elsevier, Amsterdam, 2006.
[11] F. Rodríguez-Reinoso, Carbon 36 (1998) 159–175.
[12] J.J. Bravo-Suárez, R.V. Chaudhari, B. Subramaniam, in: J.J. Bravo-Suárez, M.K. Kidder, V. Schwartz (Eds.), Novel Materials for Catalysis and Fuel Processing, American Chemical Society, Division of Energy and Fuels, Washington, 2013, pp. 3–68.
[13] A. Barroso-Bogeat, M. Alexandre-Franco, C. Fernández-González, V. Gómez-Serrano, Fuel Process. Technol. 126 (2014) 95–103.
[14] J.S. Choi, T.H. Kim, K.Y. Choo, J.S. Sung, M.B. Saidutta, S.O. Ryu, S.D. Song, B. Ramachandra, Y.W. Rhee, Appl. Catal. A 290 (2005) 1–8.
[15] J.S. Choi, T.H. Kim, K.Y. Choo, J.S. Sung, M.B. Saidutta, S.D. Song, Y.W. Rhee, J. Porous Mater. 12 (2005) 301–310.
[16] P. Michorczyk, P. Kustrowski, L. Chmielarz, J. Ogonowski, React. Kinet. Catal. Lett. 82 (2004) 121–130.
[17] B. Sreedhar, V. Bhaskar, Ch Sridhar, T. Srinivas, L. Kótai, K. Szentmihályi, J. Molec. Catal. A 191 (2003) 141–147.
[18] J. Chaichanawong, T. Yamamoto, T. Ohmori, A. Endo, Chem. Eng. J. 165 (2010) 218–224.
[19] N.K. Park, J.D. Lee, T.J. Lee, S.O. Ryu, C.H. Chang, Fuel 84 (2005) 2165–2171.
[20] S.P. Hernández, M. Chiappero, N. Russo, D. Fino, Chem. Eng. J. 176–177 (2011) 272–279.
[21] A.F. Pérez-Cadenas, C. Moreno-Castilla, F.J. Maldonado-Hódar, J.L.G. Fierro, J. Catal. 217 (2003) 30–37.
[22] M.A. Álvarez-Merino, F. Carrasco-Marín, J.L.G. Fierro, C. Moreno-Castilla, J. Catal. 192 (2000) 363–373.
[23] M.A. Álvarez-Merino, F. Carrasco-Marín, C. Moreno-Castilla, J. Catal. 192 (2000) 374–380.
[24] C. Moreno-Castilla, M.A. Álvarez-Merino, F. Carrasco-Marín, React. Kinet. Catal. Lett. 71 (2000) 137–142.
[25] M.A. Álvarez-Merino, M.F. Ribeiro, J.M. Silva, F. Carrasco-Marín, F.J. Maldonado-Hódar, Environm. Sci. Technol. 38 (2004) 4664–4670.
[26] C. Moreno-Castilla, M.A. Álvarez-Merino, F. Carrasco-Marín, J.L.G. Fierro, Langmuir 17 (2001) 1752–1756.
[27] S.E. Iyuke, F.R. Ahmadun, Appl. Surf. Sci. 187 (2002) 37–44.
[28] F.S. Baltacioğlu, B. Gülyüz, A.E. Aksoylu, Z.I. Önsan, Turk J. Chem. 31 (2007) 455–464.
[29] P.M. Boorman, R.A. Kydd, T.S. Sorensen, K. Chong, J.M. Lewis, W.S. Bell, Fuel 71 (1992) 87–93.
[30] F. Liu, S. Xu, Y. Chi, D. Xue, Catal. Commun. 12 (2011) 521–524.
[31] B.D. Cullity, Elements of X-ray Diffraction, Addison-Wesley, Reading, MA, 1959.
[32] C.S. Castro, M.C. Guerreiro, L.C.A. Oliveira, M. Gonçalves, A.S. Anastácio, M. Nazzarro, Appl. Catal. A 367 (2009) 53–58.
[33] M.A. Schettino Jr., J.C.C. Freitas, A.G. Cunha, F.G. Emmerich, A.B. Soares, P.R.N. Silva, Quim. Nova 39 (2007) 1663–1668.
[34] S. Błażewicz, A. Świątkowski, B.J. Trznadel, Carbon 37 (1999) 693–700.
[35] J.C. Arrebola, A. Caballero, L. Hernán, J. Morales, M. Olivares-Marín, V. Gómez-Serrano, J. Electrochem. Soc. 157 (2010) A791–A797.
[36] C.F. Baes Jr., R.E. Mesmer, The Hydrolysis of Cations, John Wiley & Sons, New York, 1976.
[37] D.R. Lide (Ed.), CRC Handbook of Chemistry and Physics, eighty sixth ed., Taylor & Francis, Boca Ratón, Florida, 2005.
[38] H. Remy, Treatise on Inorganic Chemistry, Vol. 1, Elsevier, Amsterdam, 1956.
[39] J. Emsley, The Elements, Clarendon Press, Oxford, 1989.
[40] R. Dobrowolski, M. Otto, Chemosphere 90 (2013) 683–690.
[41] E. Deliyanni, T.J. Bandosz, J. Hazard. Mater. 186 (2011) 667–674.
[42] M. Gonçalves, M.C. Guerreiro, L.C.A. de Oliveira, C.S. de Castro, J. Environ. Manage 127 (2013) 206–211.
[43] M.F. Al-Khatib, S.E. Iyuke, A.B. Mohamad, W.R.W. Daud, A.A.H. Kadhum, A.M. Shariff, M.A. Yarmo, Carbon 40 (2002) 1929–1936.
[44] H.R. Oswald, R. Asper, in: R.M.A. Lieth (Ed.), Preparation and Crystal Growth of Materials with Layered Structures, Kluwer Academic Publishers, Dordrecht, 1977, pp. 71–140.
[45] A.S. Shaporev, V.K. Ivanov, A.E. Baranchikov, O.S. Polezhaeva, Y.D. Tret'yakov, Russ. J. Inorg. Chem. 52 (2007) 1811–1816.
[46] E. Tchomgui-Kamga, V. Alonzo, C.P. Nanseu-Njiki, N. Audebrand, E. Ngameni, A. Darchen, Carbon 48 (2010) 333–343.
[47] B.C. Lippens, J.H. de Boer, Acta Crystallogr. 17 (1964) 1312–1321.
[48] M. Digne, P. Sautet, P. Raybaud, H. Toulhoat, E. Artacho, J. Phys. Chem. B 106 (2002) 5155–5162.
[49] X. Du, X. Su, Y. Wang, J. Li, Mater. Res. Bull. 44 (2009) 660–665.
[50] C.J. Goss, Miner. Mag. 51 (1987) 437–451.
[51] F. Watari, P. Delavignette, V. van Landuyt, S. Amelinckx, J. Solid State Chem. 48 (1983) 49–64.
[52] Ö. Özdemir, D.J. Dunlop, Earth Planet Sci. Lett. 177 (2000) 59–67.
[53] J. Lima-de-Faria, Acta Crystallogr. 23 (1967) 733–736.
[54] R.M. Cornell, U. Schwertmann, The Iron Oxides: Structure, Properties, Reactions, Occurrences and Uses, Wiley VCH, Weinheim, 2003.
[55] R. Padilla, The Reduction of Cassiterite with Carbon, Ph.D. Thesis, University of Utah, 1977.
[56] J.C. Platteeuw, G. Meyer, Trans. Faraday Soc. 52 (1956) 1066–1073.
[57] E. Wilberg, A.F. Hollemann, Inorganic Chemistry, Academic Press, San Diego, 2001.
[58] Cs. Balázsi, M. Farkas-Jahnke, I. Kotsis, L. Petrás, J. Pfeifer, Solid State Ionics 141–142 (2001) 411–416.
[59] G.N. Kustova, Y.A. Chesalov, L.M. Plyasova, I.Y. Lin, A.I. Nizovskii, Vib. Spectrosc. 55 (2011) 235–240.
[60] B. Gerand, G. Nowogrocki, J. Guenot, M. Figlarz, J. Solid State Chem. 29 (1979) 429–434.
[61] J.C. Bailar, H.J. Emeléus, R. Nyholm, A.F. Trotman-Dickenson, Comprehensive Inorganic Chemistry, Vol. 3, Pergamon Press, Oxford, 1973.
[62] M.F. Daniel, B. Desbat, J.C. Lassegues, B. Gerand, M. Figlarz, J. Solid State Chem. 67 (1987) 235–247.
[63] D.J.G. Ives, Principles of the Extraction of Metals, Royal Institute of Chemistry, London, 1960.
[64] T.B. Reed, Free Energy of Formation of Binary Compounds, MIT Press, Cambridge, 1971.
[65] Y. Ao, J. Xu, X. Shen, D. Fu, C. Yuan, J. Hazard. Mater. 160 (2008) 295–300.
[66] C.S. Castro, M.C. Guerreiro, M. Gonçalves, L.C.A. Oliveira, A.S. Anastácio, J. Hazard. Mater. 164 (2009) 609–614.
[67] Q.L. Zhang, Y.C. Lin, X. Chen, N.Y. Gao, J. Hazard. Mater. 148 (2007) 671–678.
[68] A. Quintanilla, N. Menéndez, J. Tornero, J.A. Casas, J.J. Rodríguez, Appl. Catal. B 81 (2008) 105–114.
[69] J. Yang, T. Mori, M. Kuwabara, ISIJ Int. 47 (2007) 1394–1400.
[70] R. Padilla, H.Y. Sohn, Metall. Trans. B 10 (1979) 109–115.
[71] B. Tryba, A.W. Morawski, M. Inagaki, Appl. Catal. B 41 (2003) 427–433.
[72] S. Yao, J. Li, Z. Shi, Particuology 8 (2010) 272–278.
[73] A. Mills, S. Le Hunte, J. Photochem. Photobiol. A 108 (1997) 1–35.
[74] http://webmineral.com/data/Anatase.shtml#.U-OituN_vfc.
[75] http://webmineral.com/data/Rutile.shtml#.U-OjmON_vfc.
[76] D.S. Venables, M.E. Brown, Thermochim. Acta 282/283 (1996) 251–264.
[77] D.S. Venables, M.E. Brown, Thermochim. Acta 282/283 (1996) 265–276.
[78] G.A. Swift, R. Koc, J. Mater. Sci. 36 (2001) 803–806.